Dynamics and Properties of the Cohesive Zone in Rapid Fracture and Friction

Neri Berman, Gil Cohen, and Jay Fineberg*
The Racah Institute of Physics, The Hebrew University of Jerusalem, Jerusalem 91904, Israel

(Received 18 March 2020; revised 28 June 2020; accepted 12 August 2020; published 17 September 2020)

The cohesive zone is the elusive region in which material fracture takes place. Here, the putatively singular stresses at a crack's tip are regularized. We present experiments, performed on PMMA, in which we visualize the cohesive zone of frictional ruptures as they propagate. Identical to shear cracks, these ruptures range from slow velocities to nearly the limiting speeds of cracks. We reveal that the cohesive zone is a dynamic quantity; its spatial form undergoes a sharp transition between distinct phases at a critical velocity. The structure of these phases provides an important window into material properties under the extreme conditions that occur during fracture.

DOI: 10.1103/PhysRevLett.125.125503

When two bodies are in contact and subjected to an external shear force, the myriad discrete contacts that compose the interface separating them will lose stability via a rupture front that precedes frictional sliding [1]. These frictional ruptures, once residual stresses are subtracted, have been shown to be classical shear (mode II) cracks with singular stress fields at their tip [2–4]. Once residual stresses are subtracted, dissipation in the wake of the crack can be neglected and energy balance governs their equation of motion [5], as predicted by linear elastic fracture mechanics (LEFM). LEFM predicts the singular relation for *all* cracks, $\sigma_{ij} \propto r^{-1/2}$, between stresses and the distance, r, to their tips. This divergence, as $r \to 0$, must break down in the close vicinity of a crack's tip, where materials are no longer linear [6] or even elastic. The concept of a cohesive zone is generally used to introduce a finite region where energy is dissipated, and the singularity is regularized [7–9]. Implementing cohesive zone models, theoretical modeling [2,10–14] as well as numerous numerical calculations [15] have been performed. Very few experiments, however, exist [16,17] in which the cohesive zone has actually been measured. To our knowledge, no direct measurements of this elusive region in *dynamic* fracture have ever been performed.

The difficulty in measuring the cohesive zone of a *dynamic* crack arises due to its rapid propagation velocity and extremely small size. Moreover, locating the cohesive zone with sufficient precision to resolve it has been, technically, nearly impossible. These difficulties can be circumvented by using frictional cracks, as their path is confined to the plane of frictional contact. Previous studies [3,18,19] of frictional cracks resolved the elastic fields of dynamic cracks only at distances where singular LEFM fields dominate. Since a frictional crack's trajectory is known, *a priori*, near-field measurements at the necessary spatial and temporal resolution to resolve the cohesive zone become possible. We use this to measure the cohesive zone of dynamic cracks whose velocities, C_f, range from $C_f \approx 0$ to the limiting Rayleigh wave speed, C_R. The cohesive zones studied are dynamic entities that transition, as C_f increases, between two distinct material phases. This, unanticipated, microscopic behavior has macroscopic consequences.

Experiments were conducted on poly(methylmethacrylate) (PMMA) blocks (density 1170 kg/m^3) having x, y, z dimensions 150,100,5.5 mm (upper) and 300,30,30 mm (lower) [Fig. 1(a)]. Rayleigh, shear, and longitudinal wave speeds are, respectively, $C_R \approx 1255\,\frac{m}{s}$, $C_S \approx 1345\,\frac{m}{s}$, and $C_L \approx 2680\,\frac{m}{s}$ (plane strain, using the dynamic value of the Young's modulus, $E = 5.75 \pm 2.6\%$ GPa) [3]. Both blocks were first loaded with a normal force $F_N \approx 5000$ N in the $-\hat{y}$ direction. Shear forces, F_S, were then applied quasistatically to the bottom block in the $-\hat{x}$ direction, until obtaining desired values. At this point, cracks were nucleated by imposing a small ($\sim 10^{-2} F_S$) an out-of-plane shear perturbation (mode III) in the z direction, at $x \approx 0$. Twelve to fifteen miniature (Vishay 01RJ) rosette strain gages continuously measured all components of the local 2D strain tensor, $\varepsilon_{ij}(x,t)$, 3.5 mm above the interface [black squares, Fig. 1(a)] at a 1 MHz rate. Simultaneous optical measurements of the local displacement, $u_x(x,t)$, and the real contact area, $A(x,t)$ were performed. $u_x(x,t)$ were measured by following the edges of grooves engraved on the contact surface of the upper block. Groove edges, visualized by illuminating the interface at incident angles well beyond the angle of total internal reflection, were [Fig. 1(b)] tracked via cross-correlation of successive images to achieve a 0.4 μm resolution every 0.8 μ sec [camera #1 in Fig. 1(c)] as frictional ruptures traversed the measurement region (see [20]). Acquired images were averaged in the transverse z direction, resulting in a single $u_x(x,t)$ measurement per groove edge [see Fig. 1(d)]. A second optical system illuminated the entire interface at the

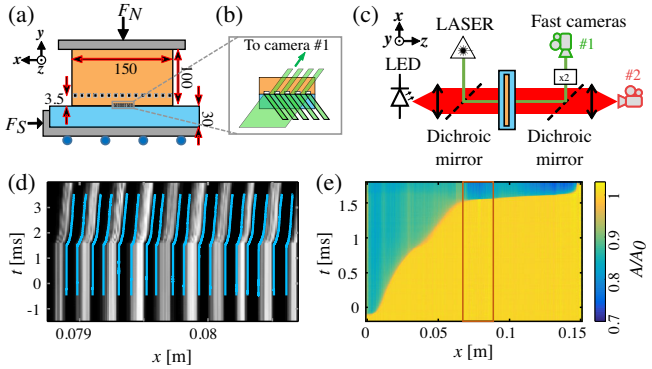

FIG. 1. Experimental system and data acquisition. (a) Schematic of the experimental system. Normal F_N and shear F_S forces are applied to PMMA blocks. Rosette-type strain gauges, mounted 3.5 mm above the interface, enable instantaneous strain measurements. Local material displacements *on* the interface are measured via grooves engraved on the upper block's contacting surface. (b) Groove edge locations are imaged by total internal reflection [1] each 0.8 μ sec [20]. (c) Separate light sources simultaneously image the real area of contact, $A(x,t)$ of the (i) groove edge displacements, $u_x(t)$, and (ii) frictional crack dynamics over the entire 150 mm interface every 1.6 μ sec. Each optical path is imaged by a separate fast camera producing simultaneous measurements of $u_x(t, y = 0)$ and C_f. (d) Typical measurements of $u_x(t)$ when averaged across the z axis. The bright (dark) borders trace $u_x(t)$ motion (blue lines) of each edge. (e) $A(x,t)$, averaged in z and normalized by $A_0 = A(x, t_0)$, where t_0 is prior to crack initiation. Colors reflect $A(x,t)/A_0$. C_f are extracted from crack tip locations, x_{tip}. Red box: grooved surface location.

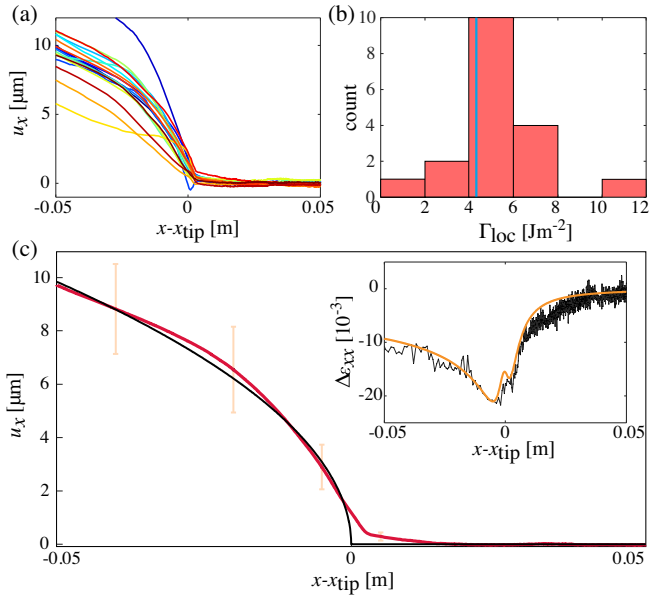

FIG. 2. Displacement measurements, u_x, on the interface for $C_f = 707\frac{m}{s}$ (0.56 C_R). (a) $u_x(t)$ [Fig. 1(d)] transformed to $u_x(x - x_{\text{tip}})$. $u_x^{(i)}(x - x_{\text{tip}})$ of the ith groove edges vary widely in amplitude for the same rupture front, each corresponding to a fracture energy, Γ_i. (b) Distribution of Γ_i from (a). Γ_i as determined by fitting $u_x^{(i)}(x - x_{\text{tip}})$ to Eq. (1). Γ_i are distributed around the value (blue line) of Γ measured by the strain gauge above the grooves. (c) The mean value of $u_x^{(i)}(x - x_{\text{tip}})$ (red) compares well to LEFM predictions (black) using Γ measured by the strain gauge. Inset: fitting the strain components to LEFM (orange curve) yields Γ at strain gage locations.

same incident angle. Under these conditions, light is transmitted only at contacting points, hence the image of the transmitted light provided the real area of contact along the entire interface [camera #2 in Fig. 1(c)] at 581 000 frames/s. Averaging in z produced real time measurements of the area of contact, $A(x,t)$. Instantaneous crack tip locations, x_{tip}, were defined as points where $A(x,t)$, normalized by $A(x, t = t_0)$, dropped by 2%. t_0 is a time slightly prior to rupture initiation. $x_{\text{tip}}(t)$ yielded C_f every 0.2 mm along the interface with a 10 m/s resolution. All measurements were synchronized by a trigger provided by an acoustic sensor mounted on the upper block at $x = 0$. We present a typical crack front measurement in Fig. 1(e).

Figure 2(a) presents superimposed measurements $u_x^{(i)}(x - x_{\text{tip}})$ of each of the $0 < i < 18$ groove edges [Fig. 1(d)] after $u_x^{(i)}(t)$ were transformed to spatial coordinates via $u_x^{(i)}(x - \int C_f dt)$. LEFM [7,8] predicts the parabolic form:

$$u_x(x - x_{\text{tip}}) \propto \sqrt{\Gamma} \cdot f(C_f) \cdot \sqrt{r}, \tag{1}$$

where Γ is the fracture energy (defined as the energy dissipated per unit crack length) and $f(C_f)$ is a known [8] kinematic function. Fitting Eq. (1) to $u_x^{(i)}(x - x_{\text{tip}})$ provides us with the value of Γ_i at each location, i. Surprisingly, Γ_i varies significantly. Figure 2(b) presents a histogram of Γ_i measured from the $u_x^{(i)}(x - x_{\text{tip}})$ in Fig. 2(a), where the blue vertical line is the value of Γ measured independently, by fitting the known angular functions of LEFM to measurements of the strain gage located above the grooves [3] [Fig. 2(c), inset]. The mean value of Γ_i coincides closely with Γ. Furthermore, the relative magnitudes of the Γ_i are approximately invariant, when comparing different events (see [20]). This suggests that Γ, as measured by strain gages, is the mean-field representation of strongly varying local values. This is illustrated [Fig. 2(c)] by the good quantitative agreement (away from x_{tip}) between the mean displacement, $u_x(x - x_{\text{tip}}) = \langle u_x^{(i)}(x - x_{\text{tip}}) \rangle_i$, and the curve predicted by LEFM using Γ. In the near vicinity of x_{tip}, however, a clear discrepancy is visible. We attribute this to the nonlinear elastic zone [6] followed by the cohesive zone at the crack's tip.

The temporal derivative of $u_x(t)$ yields the particle velocity on the interface, $v_x(x - x_{\text{tip}})$, which is one half of the slip velocity of the interface. $v_x(x - x_{\text{tip}})$ is typically

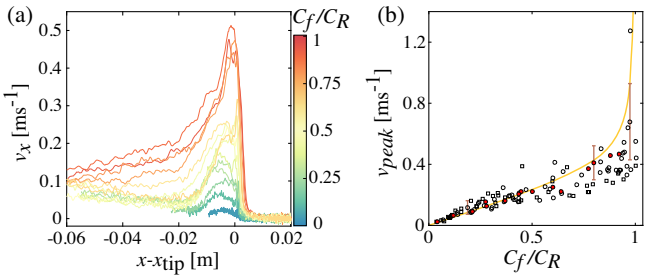

FIG. 3. Slip velocity dependence on C_f. (a) Slip velocity, $v_x(x - x_{tip})$, profiles for front velocities $0 < C_f < C_R$. v_x (see color map) increase with C_f. Measurements are prior to the return of waves reflected by system boundaries. (b) Peak slip velocity, v_{peak}, of v_x versus C_f. Marker shapes indicate different experiments, red markers denote the experiments presented in (a). Three representative error bars are displayed. Yellow line: v_{peak} versus C_f calculated from the cohesive zone model [14] in Eq. (2).

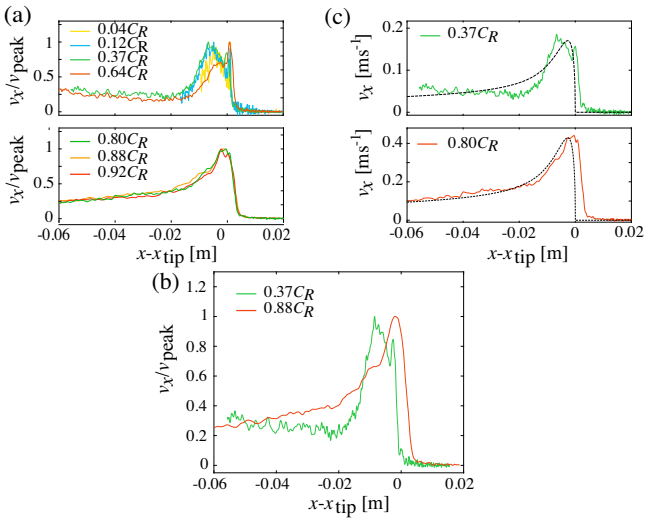

FIG. 4. Properties of the slip velocity form. (a) The two collapsed forms are qualitatively different. The high C_f regime (bottom) monotonically increases before a slow decay in v_x. In low C_f regime (top) $v_x(x)$ has a sharp local maximum followed by an abrupt increase to v_{peak} and a subsequent rapid decay in x. (b) When normalizing the slip velocity by v_{peak}, profiles collapse into two distinct forms for low and high C_f. The critical front velocity separating the two regimes is $C_c = 0.8 \pm 0.06C_R$. (c) Comparison of the two regimes to the cohesive zone model used in Fig. 3(b). The model, using $x_c = 3.2$ mm and $\Gamma = 3.5\ Jm^{-2}$, provides a reasonable description only behind the crack tip for $C_f > C_c$. In the $C_f < C_c$ regime, this simple model fails for all x. Note that the distance between the points in each measurement presented is less than 1 μm.

three to four orders of magnitude below C_f [25–27]. As $v_x(x_{tip})$ of the LEFM solution is putatively singular, the amplitude, spatial scale, and form of $v_x(x)$ in the vicinity of x_{tip} characterize the cohesive zone, where the singularity is regularized. Figure 3(a) presents multiple measurements of $v_x(x - x_{tip})$ for $0 < C_f < C_R$. Their peak velocities, v_{peak}, nonlinearly increase with C_f as shown in Fig. 3(b). This behavior is qualitatively described by a slip-weakening cohesive zone model presented in [14], which assumes a gradual decrease of shear stresses, $\tau(x)$, as with the distance from the crack tip:

$$\tau(x) = (\tau_p - \tau_r)\tilde{\tau}(x/x_c) + \tau_r, \tag{2}$$

where τ_p, τ_r, x_c are the peak stress, residual stress, and cohesive length, respectively. For simplicity, we chose $\tilde{\tau}(x) = \exp(-x)$.

Using Eq. (2), we are able to obtain $v_x(x - x_{tip})$ as follows (see [20]). As in [7,8], we solve the elastic equations by assuming a steadily moving crack. Following [14], we impose boundary conditions containing the stress profile as described in Eq. (2) for the cohesive zone, and the known boundary conditions for a mode II crack outside the cohesive zone (see [7,8]). The solution of these equations results in the entire strain field, ε_{ij}, which can be explicitly calculated for $y = 0$. Particle velocities are then obtained by the relation to the crack velocity $v_x(x) = -C_f \cdot \varepsilon_{xx}(x, y = 0)$. The value of $x_c \sim 3$ mm is obtained by comparison of the calculated $v_x(x - x_{tip})$ to measurements. Although the model may adequately describe v_{peak} as a function of C_f, we will show that it does not describe the functional form of $v_x(x)$ well.

Figure 4(a) presents measured spatial profiles of v_x/v_{peak} for different C_f. Surprisingly, the data collapse into two distinct profiles according to high or low C_f. A transition between the two takes place at $C_f = C_c = 0.8 \pm 0.06C_R$.

We compare the two profiles in Fig. 4(b). When $C_f > C_c$, v_x increases smoothly and rapidly to v_{peak} before slowly decaying. When $C_f < C_c$, v_x increases initially to a sharp local maximum, then drops sharply before increasing to v_{peak}, before rapidly decaying in space until about $0.2v_{peak}$.

Slip-weakening cohesive zone models, while able to describe $v_{peak}(C_f)$, utterly fail to describe cohesive zone profiles for $C_f < C_c$. As the comparison in Fig. 4(c) demonstrates, neither the nonmonotonic form nor width of the v_x profiles are captured by this simple model.

v_x profiles for $C_f > C_c$ however, do not fare as badly. As demonstrated in Fig. 4(c, bottom), the slow decay of v_x beyond v_{peak} is actually described quite well by Eq. (2). In both regimes, however, slip initiates ($v_x > 0$) *prior* to the crack tip's arrival. This implies that slip is already taking place prior to fracture of the contacts [defined by $A(x, t) = 0.98A(x, 0)$] within the interface. This is, of course, missing in the cohesive zone theoretical description.

The most striking feature revealed by the measurements, the sharp transition at C_c, cannot be explained by simple "static" cohesive zone models. Modeling such features will necessitate incorporating dynamic behavior within cohesive zones.

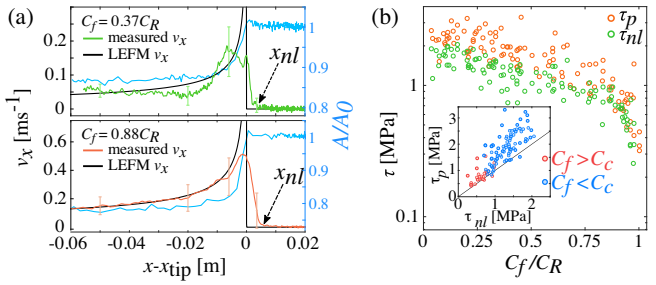

FIG. 5. Shear stress changes with C_f. (a) Comparisons of $A(x - x_{\rm tip})$ (blue), $v_x(x - x_{\rm tip})$ (green, top; red, bottom), and the LEFM solution (black) for v_x. For both $C_f < C_c$ (top) and $C_f > C_c$ (bottom) slip ($v_x > 0$) initiates upon the crack tip's arrival at $x_{\rm tip} = x_{\rm nl}$. The locations $x_{\rm nl}$ (denoted by arrows) are, therefore, the last point where the LEFM solution (hence linear elasticity) is valid. Typical error bars, resulting from v_x fluctuations [see Fig. 4 (a)], are noted. (b) Green: the C_f dependence of the shear stress value, $\tau_{\rm nl}$, at the onset of the nonlinear region defined at $x - x_{\rm tip} = x_{\rm nl}$, where the LEFM solution starts to break down. Red: C_f dependence of the peak shear stress of the cohesive zone, τ_p, calculated with the cohesive zone model, Eq. (2) [14] at the measured $v_{\rm peak}$. Both quantities exhibit similar behavior, with a clear transition at $C_f \approx C_c$. Both τ_p and $\tau_{\rm nl}$ vs $v_{\rm peak}$ are presented in [20]. Inset: solid line indicates equality. While τ_p is greater than $\tau_{\rm nl}$ for $C_f < C_c$, beyond C_c their values coincide.

Figure 5(a), presents a simultaneous comparison of $A(x - x_{\rm tip})$, $v_x(x - x_{\rm tip})$, and the corresponding LEFM predictions for each regime. The figure clearly demonstrates that slip initiates prior to any reduction of $A(x, t)$. This indicates that the first action performed by the crack is a process other than contact separation. This "preslip" must be a nonlinear or plastic process, as linear elastic processes are fully incorporated into LEFM, which predicts that no slip should precede the tip.

We now utilize the LEFM solution to measure the value of the shear stress at the point, $x_{\rm nl}$, where slip initiates. We will assume (as demonstrated by [3,28]) that the LEFM solution is accurate for all $x > x_{\rm nl}$, whereas at this point nonlinear behavior will ensue. The LEFM solution therefore provides us with an accurate measure of the maximal value of the linear elastic shear stress, $\tau_{\rm nl} \equiv \tau^{(\rm LEFM)}(x_{\rm nl}, y = 0)$, where $\tau^{(\rm LEFM)}$ is the value at $x_{\rm nl}$ provided by LEFM. $\tau_{\rm nl}$ is the shear stress at which the material begins to soften, via either nonlinear elastic or plastic deformation (see [20]).

Figure 5(b) describes both the variation of $\tau_{\rm nl}$ with C_f and compares $\tau_{\rm nl}$ to the maximal peak stress on the interface, τ_p, as calculated from the cohesive zone model [Eq. (2)] at $\tau_p(x_{\rm peak})$. The data were obtained from numerous different experiments and provide a clear picture. First, for all C_f, both τ_p and $\tau_{\rm nl}$ track each other well. Furthermore, as we would expect, $\tau_p \geq \tau_{\rm nl}$ over the entire C_f range. Both τ_p and $\tau_{\rm nl}$ describe a gradual decline with C_f, implying shear weakening of the interface for $C_f < C_c$. Notably, Fig. 5(b) also demonstrates that both $\tau_{\rm nl}$ and τ_p undergo a distinct transition at $C_f/C_R \approx 0.84$ to a regime of rapidly dropping values. C_c is approximately the same velocity where both the residual strain and residual contact area decrease sharply as shown in [26]. The sharp kink at the transition, which is evident in both curves, corresponds to $C_f \sim C_c$, the front velocity separating the different cohesive zones forms (Fig. 4). Beyond C_c, $\tau_{\rm nl}$ and τ_p nearly coincide [inset of Fig. 5(b)].

Our measurements go far beyond the results of previous work [3,5,26,28] where "far field" behavior was compared to LEFM, as they probe the structure of precisely the region that LEFM, by definition, cannot describe. The transition at C_c, however, corresponds closely to that noted in [26] where the frictional resistance and residual contact area changed their behavior. It is interesting that these velocities also roughly correspond to strong digressions of the shear strain from LEFM predictions [3]. Beyond a detailed description of how the singular region near a crack's tip breaks down, our measurements of the cohesive zone contain a number of surprises. The most important of these is that the cohesive zone is not a passive entity but, instead, undergoes dynamic behavior; at a critical velocity, both its functional form and characteristic properties change their character at a sharp transition.

Let us first consider the mechanism driving this transition. A possible explanation may be provided by a type of flash heating mechanism [29] in which the crack is propagating so quickly that the energy (Γ) deposited within the cohesive zone will have insufficient time to be thermally conducted away. Under these circumstances, material temperatures will increase to a point that the character of the material undergoing fracture fundamentally changes. In our case, a simple thermal model (see [20]) predicts that, beyond C_c, the PMMA will be heated beyond its glass temperature and will therefore soften. Evidence for this has been suggested in [26,27] for both PMMA and Homalite [25]. While the details of these observations may only characterize thermo-plastics, since flash heating [29] is a general mechanism, we believe that nontrivial cohesive zone dynamics may well take place in other materials. The specific form that these dynamics will take in rock or engineering materials has yet to be studied.

Direct evidence for extreme softening within the cohesive zone beyond C_c is also provided by Figs. 3 and 5. Only beyond C_c does $\tau_{\rm nl} = \tau_p$ [Fig. 5(b)], suggesting elastic-plastic behavior within the cohesive zone. Further support for elastic-plastic behavior in this regime is provided by evidence of large strains that occur precisely where shear stresses (characterized by both $\tau_{\rm nl}$ and τ_p) drop; the relation $v_x = -C_f \cdot \varepsilon_{xx}$ [7] provides us with a direct measure of the peak strain, $\varepsilon_{xx}^{\rm peak} = v_{\rm peak}/C_f$. The sharp rise of $v_{\rm peak}$ for $C_f > C_c$ in Fig. 3 therefore strongly suggests that, beyond C_c, $\varepsilon^{\rm peak}$ increases rapidly while shear stresses decrease.

Our measurements indicate complex material behavior for $C_f < C_c$. The linear zone of Fig. 3(b) suggests nearly constant values of $\varepsilon_{xx}^{\text{peak}} = v_{\text{peak}}/C_f$ in this region. The complex form of the v_x profile for $C_f < C_c$ indicates that, in this regime, the cohesive zone has a nontrivial structure; it is significantly localized with characteristic nonmonotonic structure. The localization, when coupled with the dip in $v_x(x)$ that drops *below* that predicted by LEFM may imply material hardening in this vicinity, whereas the nonmonotonicity could imply dynamic structural changes within the highly strained material.

Our direct measurements of the cohesive zone provide a new window into material behavior at extreme strain rates and stresses. This work has illuminated, hitherto hidden, detailed material properties of the rough, submicron layer that governs the frictional resistance of this material. Material properties under the extreme conditions that take place during fracture, are nearly impossible to access. They are, however, critical to our fundamental understanding of material strengths and fracture properties—as *only* under such conditions do materials fail.

We acknowledge the support of the Israel Science Foundation (Grant No. 840/19).

*jay@mail.huji.ac.il

[1] S. M. Rubinstein, G. Cohen, and J. Fineberg, Nature (London) **430**, 1005 (2004).

[2] A. C. Palmer and J. R. Rice, Proc. R. Soc. A **332**, 527 (1973).

[3] I. Svetlizky and J. Fineberg, Nature (London) **509**, 205 (2014).

[4] F. Barras, M. Aldam, T. Roch, E. A. Brener, E. Bouchbinder, and J.-F. Molinari, Earth Planet. Sci. Lett. **531**, 115978 (2020).

[5] I. Svetlizky, D. S. Kammer, E. Bayart, G. Cohen, and J. Fineberg, Phys. Rev. Lett. **118**, 125501 (2017).

[6] E. Bouchbinder, T. Goldman, and J. Fineberg, Rep. Prog. Phys. **77**, 046501 (2014).

[7] K. B. Broberg, *Cracks and Fracture* (Academic Press, New York, 1999), ISBN 9780874216561.

[8] L. B. Freund, *Dynamic Fracture Mechanics* (Cambridge University Pressx, Cambridge, England, 1998).

[9] B. Lawn, *Fracture of Brittle Solids*, 2nd ed., Cambridge Solid State Science Series (Cambridge University Press, Cambridge, England, 1993).

[10] G. Barenblatt, Adv. Appl. Mech. **7**, 55 (1962).

[11] Y. Ida, J. Geophys. Res. **77**, 3796 (1972).

[12] D. Dugdale, J. Mech. Phys. Solids **8**, 100 (1960).

[13] M. Ohnaka and T. Yamashita, J. Geophys. Res. **94**, 4089 (1989).

[14] O. Samudrala, Y. Huang, and A. J. Rosakis, J. Geophys. Res. **107**, 2170 (2002).

[15] A. Needleman, Procedia IUTAM **10**, 221 (2014).

[16] F. Célarié, S. Prades, D. Bonamy, L. Ferrero, E. Bouchaud, C. Guillot, and C. Marlière, Phys. Rev. Lett. **90**, 075504 (2003).

[17] E. Guilloteau, H. Charrue, and F. Creuzet, Europhys. Lett. **34**, 549 (1996).

[18] M. Mello, H. Bhat, A. J. Rosakis, and H. Kanamori, Earth Planet. Sci. Lett. **387**, 89 (2014).

[19] H. Shlomai and J. Fineberg, Nat. Commun. **7**, 11787 (2016).

[20] See the Supplemental Material at http://link.aps.org/supplemental/10.1103/PhysRevLett.125.125503 for a detailed description of the sample preparation and slip measurement method. A brief description of how the cohesive zone model was used to obtain slip velocity distributions. We also demonstrate that the relative fracture energy is a local quantity, provide both τ_p and τ_{nl} dependence with slip velocity, and include a heating-based model for the phase transition described in the text. The material includes Refs. [21–24].

[21] N. M. Beeler, T. E. Tullis, and D. L. Goldsby, J. Geophys. Res. **113**, B01401 (2008).

[22] F. X. Passelègue, D. L. Goldsby, and O. Fabbri, Geophys. Res. Lett. **41**, 828 (2014).

[23] J. H. Dieterich and B. D. Kilgore, Tectonophysics **256**, 219 (1996).

[24] F. Bowden and D. Tabor, *The Friction and Lubrication of Solids* (Oxford University Press, New York, 2001).

[25] V. Rubino, A. J. Rosakis, and N. Lapusta, Nat. Commun. **8**, 15991 (2017).

[26] I. Svetlizky, E. Bayart, G. Cohen, and J. Fineberg, Phys. Rev. Lett. **118**, 234301 (2017).

[27] O. Ben-David, G. Cohen, and J. Fineberg, Tribol. Lett. **39**, 235 (2010).

[28] E. Bayart, I. Svetlizky, and J. Fineberg, Nat. Phys. **12**, 166 (2016).

[29] J. R. Rice, J. Geophys. Res. **111**, 1 (2006).